Journal of Materials Chemistry A

PAPER

View Article Online
View Journal | View Issue

Cite this: J. Mater. Chem. A, 2017, 5, 7869

Ruthenium–nickel–nickel hydroxide nanoparticles for room temperature catalytic hydrogenation†

Lihua Zhu,*[ab] Shiyao Shan,[d] Valeri Petkov,[e] Weiwei Hu,[c] Anna Kroner,[f] Jinbao Zheng,[b] Changlin Yu,[a] Nuowei Zhang,[b] Yunhua Li,[b] Rafael Luque,*[bg] Chuan-Jian Zhong,[d] Hengqiang Ye,[c] Zhiqing Yang*[c] and Bing H. Chen*[b]

Received 15th February 2017
Accepted 27th March 2017

DOI: 10.1039/c7ta01437f

rsc.li/materials-a

Improving the utilization of metals in heterogeneous catalysts with excellent catalytic performance, high selectivity and good stability represents a major challenge. Herein a new strategy is disclosed by enabling a nanoscale synergy between a transition metal and a noble metal. A novel Ru/Ni/Ni(OH)$_2$/C catalyst, which is a hybrid of Ru nanoclusters anchored on Ni/Ni(OH)$_2$ nanoparticles (NPs), was designed, prepared and characterized. The Ru/Ni/Ni(OH)$_2$/C catalyst exhibited a remarkable catalytic activity for naphthalene hydrogenation in comparison with existing Ru/C, Ni/Ni(OH)$_2$/C and Ru–Ni alloy/C catalysts. This is mainly attributed to the interfacial Ru, Ni and Ni(OH)$_2$ sites of Ru/Ni/Ni(OH)$_2$/C, where hydrogen is adsorbed and activated on Ru while Ni transfers the activated hydrogen species (as a "bridge") to the activated naphthalene on Ni(OH)$_2$ sites, producing decalin through a highly effective pathway.

1 Introduction

Aromatic compounds are important platform chemicals in the chemical industry, with extended products from the hydrogenation of the aromatic ring being relevant for a number of applications.[1–7] For example, tetralin, octahydronaphthalene and decalin can be generated from naphthalene hydrogenation.[1] Tetralin and decalin are mainly used as grease, resin and rubber dissolving agents as well as as varnish removers and additives in lubricants, dyes, pesticides and pharmaceuticals.[8–10] Despite their extensive use in the petrochemical industry, the removal of aromatics is of great practical significance due to their inherent toxicity and carcinogenic effects.[11–13] Catalytic hydrogenation has been extensively employed for the removal of aromatics.[14] A number of heterogeneous catalysts have been employed in catalytic hydrogenation including non-noble metal catalysts (nickel-based),[15] precious metal catalysts (platinum-based,[16] palladium-based,[17] rhodium-based,[18] ruthenium-based,[19] and bimetallic-based (Pt–Pd[20])) and some novel types of catalysts such as transition metal carbides, nitrides and phosphides.[9] To the best of our knowledge, there is no reported catalyst with superior catalytic activity, high stability and low cost for arene hydrogenation under mild reaction conditions (*ca.* room temperature). Finding an optimal way to design and develop low-cost, highly efficient and selective nanocatalysts for naphthalene hydrogenation at room temperature is significant not only for fundamental research but also for potential industrial applications.

Synergistic effects can significantly enhance the catalytic activity, selectivity and stability of multi-metallic catalysts.[21–24] Taking catalytic oxidation reactions as an example, Yates *et al.*[25] found that CO oxidation could be promoted by efficiently using Au/TiO$_2$ with the excellent catalytic performance attributed to the synergetic effect of Au–Ti interface and TiO$_2$. CO and O$_2$ were more easily activated on TiO$_2$ and Au–Ti interfaces, respectively. This synergistic effect of multiple active sites was also present in various multi-metallic nanocatalysts for hydrogenation reactions such as tetralin hydrogenation over Pt–Ni/AC[26] and benzene hydrogenation over Pd/C and [bmim]Cl–AlCl$_3$.[27] Additionally, hybrid nanomaterials have been widely used in the fields of catalysis, energy conversion and storage, *etc.* For example, Schaak's group successfully prepared the Ag–Pt–Fe$_3$O$_4$ heterotrimer isomer and further investigated the

[a]School of Metallurgy and Chemical Engineering, Jiangxi University of Science and Technology, Ganzhou 341000, Jiang Xi, China

[b]Department of Chemical and Biochemical Engineering, National Engineering Laboratory for Green Productions of Alcohols-Ethers-Esters, College of Chemistry and Chemical Engineering, Xiamen University, Xiamen 361005, China. E-mail: lihuazhu@stu.xmu.edu.cn; chenbh@xmu.edu.cn; Fax: +86-592-2184822

[c]Shenyang National Laboratory for Materials Science, Institute of Metal Research, Chinese Academy of Sciences, Shenyang 110016, China. E-mail: yangzq@imr.ac.cn

[d]Department of Chemistry, State University of New York at Binghamton, Binghamton, New York 13902, USA

[e]Department of Physics, Central Michigan University, Mt. Pleasant, Michigan 48859, USA

[f]Diamond Light Source, Diamond House, Harwell Science and Innovation Campus, Chilton, Oxfordshire, OX11 0DE, UK

[g]Departamento de Química Orgánica, Universidad de Córdoba, Campus de Rabanales, Edificio Marie Curie (C-3), Ctra Nnal IV, Km 396, E14071, Córdoba, Spain. E-mail: q62alsor@uco.es

† Electronic supplementary information (ESI) available: Synthetic details, TEM, XRD, XPS, some HAADF-STEM images, EDS elemental mapping, EDS line-scan results and HEXRD results of the catalysts, and catalytic performance of catalysts reported in the literature. See DOI: 10.1039/c7ta01437f

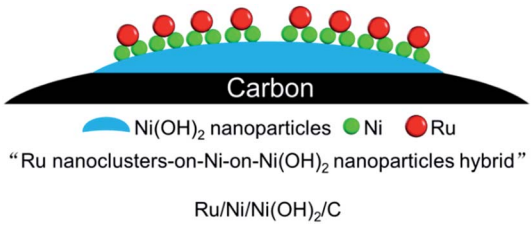

Scheme 1 Design of the ruthenium nanoclusters-on-nickel-on-nickel hydroxide nanoparticle hybrid (Ru/Ni/Ni(OH)$_2$/C).

formation mechanism of the Ag–Pt–Fe_3O_4 heterotrimer.[28,29] In this study, the Ru/Ni/Ni(OH)$_2$/C nanocatalyst with the hybrid nanostructure of ruthenium-on-nickel-on-nickel hydroxide NPs was designed and prepared with synergetic multiple catalytic sites (Scheme 1). This nanostructure was proved by a variety of techniques including high-resolution transmission electron microscopy (HRTEM), high angle annular dark field-scanning transmission electron microscopy (HAADF-STEM), EDS elemental mapping and line-scans, high-sensitivity low-energy ion scattering (HS-LEIS), synchrotron high-energy XRD (HE-XRD) and X-ray absorption spectroscopy (XAS). The catalytic performance of Ru/Ni/Ni(OH)$_2$/C was tested for the selective hydrogenation of naphthalene, and it exhibited high catalytic activity and ~100% selectivity to decalin. These structural investigations provide important information for understanding the origin of the excellent performance of the Ru/Ni/Ni(OH)$_2$ nanocatalyst.

2 Experimental

The catalyst support, carbon black (BLACK PEARLS 2000 LOT-1366221), was purchased from Cabot Corporation. All other reagents, including nickel(II) chloride hexahydrate ($NiCl_2 \cdot 6H_2O$), anhydrous ethanol, sodium hydroxide (NaOH), anhydrous ruthenium chloride ($RuCl_3$), 85 wt% (weight percent) hydrazine hydrate solution, tetralin, decalin and naphthalene, were obtained from Sinopharm Chemical Reagent Co. Ltd. (Shanghai, China). The water used in this study was deionized water. All chemicals were used as received.

Ni/Ni(OH)$_2$/C was prepared at room temperature (RT) *via* a hydrazine hydrate reduction method, with a Ni (total Ni element) loading of 12.3 wt%. The synthesis details are as follows: a certain amount of nickel chloride hexahydrate ($NiCl_2 \cdot 6H_2O$, 0.9000 g) was dissolved in a mixture of 82.5 mL of deionized water and 12.5 mL of anhydrous ethanol (adjust the dielectric constant of solution) and magnetically stirred at RT for ten minutes. And then NaOH (1.813 g) was dissolved in 12.5 mL of deionized water, forming an aqueous NaOH solution. This aqueous NaOH solution was immediately added into the above solution. Ten minutes later, the addition of 25 mL of 85 wt% hydrazine hydrate solution was performed. Subsequently, 1.250 g of carbon black was added to the above mixture after ten minutes, which was then transferred into an autoclave (Parr 4848). The mixture was magnetically stirred at RT for 18 hours. The solid sample was collected and washed with deionized water and anhydrous ethanol, and then dried in a vacuum oven at 60 °C for 6 h. The Ru/Ni/Ni(OH)$_2$/C catalyst was obtained by galvanic replacement with Ni/Ni(OH)$_2$/C,[30–37] with 7.5 wt% Ru and 6.0 wt% Ni loading. A calculated amount of an aqueous solution of $RuCl_3$ (9.64×10^{-3} mol L^{-1}) was added to the above as-prepared solid sample (Ni/Ni(OH)$_2$/C – 0.3000 g) under vigorous stirring for 6 h. And then a black powder was collected by filtration, which was thoroughly washed with deionized water and anhydrous ethanol. The fresh catalyst (Ru/Ni/Ni(OH)$_2$/C) was obtained after drying in a vacuum oven at 60 °C for 6 h. Ni/NiO/C was obtained after Ni/Ni(OH)$_2$/C was calcined under a N_2 flow of 80 mL min^{-1} at 380 °C for 2 h, with a heating rate of 2 °C min^{-1}. Ru/Ni/NiO/C with a 7.5 wt% Ru content was formed by galvanic replacement with the Ni/NiO/C sample – a certain amount of an aqueous solution of $RuCl_3$ (9.64×10^{-3} mol L^{-1}) was added to 0.3000 g of Ni/NiO/C. For comparison, 7.5 wt% Ru/C was synthesized *via* incipient wetness impregnation and then annealed under a N_2 + 10% H_2 flow of 80 mL min^{-1} at 380 °C for 3 h, with a heating rate of 2 °C min^{-1}. The chemical compositions of the catalysts were analyzed by inductively coupled plasma atomic mass spectrometry by using an Agilent ICP-MS 4500-300.

The crystallite phase of Ni in the catalysts was analyzed by the powder X-ray diffraction (XRD) technique by using a Rigaku X-ray diffractometer equipped with a high-speed array detection system. Cu Kα radiation (40 kV and 30 mA) was used as the X-ray source. The scanning 2θ range was 10–90°. The chemical state and surface composition of Ru and Ni species were determined by X-ray photoelectron spectra (XPS) on a PHI Quantum 2000 Scanning ESCA Microprobe, with monochromatic Al Kα radiation (1846.6 eV) as the X-ray source. Transmission electron microscope (TEM) and high-resolution TEM (HRTEM) measurements of the samples were performed on a Tecnai F30 electron microscope with an accelerating voltage of 300 kV. HAADF-STEM images, EDS elemental mapping and line-scan profile results were obtained by using a Tecnai F30 electron microscope. The electron beam size was below 2.0 nm, which was used for EDS elemental mapping and line-scan. The acquisition time for EDS spectra for individual particles is usually above 10 s, while that for each step of line-scan and two-dimensional mapping is 1.0 s. The EDS spectra provided the chemical composition of Ru and Ni in the catalyst, while the EDS line-scan profiles and elemental mapping were used to analyze the variation of Ru or Ni element. Because the Ru–Ni bimetallic nanoparticles (BNPs) were very small and the EDS counts were relatively low, all the EDS elemental test results are qualitative, rather than quantitative. HS-LEIS tests of the samples were conducted on an IonTOF Qtac100 low-energy ion scattering analyzer, with a $^{20}Ne^+$ beam energy of 5 keV and a sample current of 1.6 nA.

High-Energy XRD (HE-XRD) measurements were carried out at beamline 11-ID-B at the Advanced Photon Source, Argonne National Laboratory, using X-rays with an energy of 115 keV (wavelength, λ = 0.1080 Å). Samples were measured at room temperature in an ambient atmosphere. HE-XRD patterns were reduced to the so-called atomic PDFs $G(r)$. By their nature, PDFs oscillate around zero and show positive peaks at real space

distances, r, where the local atomic density $\rho(r)$ exceeds the average one ρ_o. More precisely, $G(r) = 4\pi r\rho_o[\rho(r)/\rho_o - 1]$, where $\rho(r)$ and ρ_o are the local and average atomic number densities, respectively. High-energy XRD and atomic PDFs have already proven to be very efficient for studying the atomic-scale structure of nanosized materials.[38]

The XAS experiment was carried out on beamline B18 at Diamond Light Source. B18 is a bending magnet beamline which has been designed to deliver monochromatic X-rays in the energy range of 2 to 35 keV. The beamline was set up on the Pt-coated branch and with a Si(311) monochromator. The beam was defocused up to a dimension slightly lower than 1 × 1 mm. All of the samples were measured as received without mixing with any diluting material. Prior to the measurement the samples were pressed into 12 mm diameter pellets.

The Ru XAS measurements were performed in transmission mode using ionization chambers I_0 that measures intensity of the beam before it passes through the sample and I_t that records the intensity of the beam after X-ray penetration through the sample. The Ni K-edge XAS measurements were performed in fluorescence mode using a high count rate fluorescence 36 element germanium detector. For each sample, a scan was performed to optimize the position of the sample in the beam and then six XAS scans were acquired. The acquisition time of a single XAS spectrum was *ca.* 5 minutes. Ru K-edge XAS spectra were collected in the energy range of 21 910–23 100 eV which corresponds to about −220–970 eV with respect to the edge. Ni K-edge XAS spectra were collected in the energy range of 8130–9335 eV which corresponds to about −215–990 eV with respect to the edge. The energy step in the whole XAS region was 0.5 eV. The energy was calibrated at the Ru K-edge and Ni K-edge by measuring metal foils of Ru and Ni alongside the XAS measurement of the sample, respectively.

All of the data reduction and XANES analysis were carried out by using ATHENA, a program for XAS data processing.[39] During the data processing, two scans from the same sample were merged and used for the analysis. The data processing was done in a standard manner: the raw data were calibrated and the best-fit pre-edge and post-edge background removed, summed and normalized by setting the edge step to 1. The edge position was determined from the derivative of the normalized data, with the first maximum peak after the pre-edge region in this spectrum considered to be the main absorption energy.

The program Artemis[40] was used to model the oscillations in the Extended X-ray Absorption Fine Structure (EXAFS) spectra and to determine the structural parameters of the Ru and Ni coordination environment. The phase shifts corresponding to the photoelectron waves associated with the central atom and potential surrounding atoms were calculated by *ab initio* methods, using a muffin tin approximation.

Typically, the naphthalene hydrogenation reaction was conducted in the autoclave (Parr 4848). Firstly, the mixture of catalyst (0.050 g) and cyclohexane naphthalene solution (30 mL) (wt% = 3.02%) was fed into the reactor. And then air in the reactor was replaced with N_2 and H_2 for 1 min, sequentially. Secondly, hydrogen was introduced into the reactor until the pressure reached 4.8 MPa at RT. The reactor was quickly heated to the desired reaction temperature. After the reaction was maintained for the indicated time at a mechanical agitation speed of 500 rpm, the reactor was stopped and quickly cooled to about 5 °C in an ice-water bath. Subsequently, hydrogen was released and the reaction liquid was obtained by centrifugation. The products were analyzed using a gas chromatograph (Shimadzu GC 2010) equipped with a DB-35 60 m × 0.32 mm capillary column and a flame ionization detector (FID), and gas chromatography-mass spectrometry (Shimadzu GC-MS 2010). The turnover frequency (TOF) of the catalyst was calculated on the basis of the moles of total Ru metal. The measurement of metal dispersion was not conducted for most of the unsupported or supported catalysts for the liquid naphthalene hydrogenation in the reported references (as shown in Table S1†), and the Ni element in the catalysts was mainly in the oxidized state. Therefore, with the purpose of comparing the results of this work with the references, the metal dispersion (D) of the catalysts was not investigated in this work.

3 Results and discussion

3.1 Selective catalytic hydrogenation of naphthalene

The catalytic activity of the catalysts was tested for the selective hydrogenation of naphthalene. Table 1 summarizes the catalytic properties of the synthesized catalytic systems. Ru/Ni/$Ni(OH)_2$/C efficiently catalyzed naphthalene hydrogenation (>99% conversion, 158.8 h^{-1} TOF) with a high selectivity to decalin (>90%) at 100 °C for 0.5 h (Table 1, entry 1). Naphthalene was totally hydrogenated to decalin within 1 h (TOF = 80 h^{-1}) (Table 1, entry 2). As the reaction temperature was decreased to 80 °C, quantitative decalin yields could be obtained within 2 h (entry 3 in Table 1). Ru/Ni/$Ni(OH)_2$/C also provided 100% selectivity to decalin with complete naphthalene conversion at 40 °C within 11 h (entry 4 in Table 1). An increased weight of Ru/Ni/$Ni(OH)_2$/C (0.3 g) could provide quantitative

Table 1 Catalytic performance of the catalysts for naphthalene hydrogenation[a]

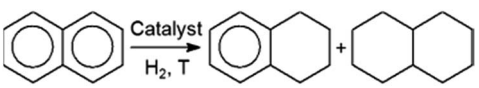

Entry	Catalyst (0.1 g)	T (°C)	t (h)	TOF (h^{-1})	Yield[b]	Yield[c]
1	Ru/Ni/$Ni(OH)_2$/C	100	0.5	158.9	<10%	90%
2	Ru/Ni/$Ni(OH)_2$/C	100	1.0	80.0	—	>99%
3	Ru/Ni/$Ni(OH)_2$/C	80	2	40.0	—	>99%
4	Ru/Ni/$Ni(OH)_2$/C	40	11	7.3	—	>99%
5	Ru/Ni/$Ni(OH)_2$/C[d]	25	13	2.1	—	>99%
6[e]	Ru/Ni/$Ni(OH)_2$/C[d]	15	75	0.4	—	>99%
7	Ru–Ni alloy/C	100	0.5	—	—	—
8	Ru/C	100	0.5	—	<15%	—
9[e]	Ru/C[d]	15	75	—	0	—

[a] Reaction conditions: cyclohexane naphthalene solution (30 mL, 3.02% weight percent naphthalene), initial H_2 pressure (4.48 MPa). Yields for Ni/$Ni(OH)_2$/C and carbon were <0.1%. [b] Yield to tetralin. [c] Yield to decalin. [d] Catalyst (0.3 g). [e] Initial H_2 pressure (1.45 MPa).

decalin yield at RT after a 13 h reaction (or at 15 °C under 1.45 MPa hydrogen and within 75 h) (Table 1, entries 5 and 6). Importantly, virtually no conversion in the systems was observed for Ru–Ni alloy/C, Ni/Ni(OH)$_2$/C and Ru/C catalysts forcing the reaction conditions (4.48 MPa, 100 °C and 0.5 h, Table 1, entries 7 to 9).

Based on the catalytic performance of all as-synthesized catalysts, an unprecedented catalytic activity was observed for Ru/Ni/Ni(OH)$_2$/C, remarkably improved in comparison to Ru/C, Ni/Ni(OH)$_2$/C and Ru–Ni alloy catalysts. The catalytic performance of Ru/Ni/Ni(OH)$_2$/C was further found to be unprecedented under reaction conditions similar to those of most reported supported and unsupported catalysts (Table S1†). This includes excellent catalytic activities for naphthalene hydrogenation at 15 °C, which to the best of our knowledge is the lowest reaction temperature reported in heterogeneous naphthalene hydrogenation. These results can be attributed to the synergy effect of multiple catalytically active sites (Ru, Ni and Ni(OH)$_2$). Detailed characterization of the designed catalyst was able to prove the proposed Ru/Ni synergy.

3.2 TEM and HRTEM tests of the nanocatalysts

Fig. S1† shows the TEM images and NP size distribution of different samples, pointing out the presence of nicely dispersed nanoparticles (NPs) in the materials. To investigate the nanostructure of NPs in the catalysts, HRTEM experiments were subsequently conducted. As shown in Fig. 1a, a lattice fringe with an interplanar spacing of 0.232 nm corresponded to the (101) facets of Ni(OH)$_2$. A lattice fringe with a spacing of 0.235 nm ascribed to the (100) facets of hexagonal close packed (hcp) Ru can be clearly seen in the HRTEM images of Ru/C (Fig. 1b). HRTEM images of Ru/Ni/Ni(OH)$_2$/C displayed lattice fringes of 0.235 nm and 0.232 nm (Fig. 1c), assigned to the (100) facets of hcp Ru and Ni(OH)$_2$ (101) planes, respectively. Fig. 1d depicts one HRTEM image of another nanoparticle in Ru/Ni/Ni(OH)$_2$/C, the indicated lattice fringes of 0.206 and 0.232 nm corresponding to Ru(101) and Ni(OH)$_2$(101) planes. These results demonstrate that Ni is mainly present in the form of Ni(OH)$_2$ in Ru/Ni/Ni(OH)$_2$/C, which is fully consistent with the XRD and XPS characterization results of the catalysts (Fig. S2 and S3 and Tables S2 and S3†). This also suggests that Ru particles could be in intimate contact with Ni/Ni(OH)$_2$ NPs (Ru-on-Ni/Ni(OH)$_2$ hybrid) in Ru/Ni/Ni(OH)$_2$/C. Additionally, TEM and HRTEM tests of the Ru/Ni/Ni(OH)$_2$/C catalyst were also performed, and the images are shown in Fig. S4.† It could be clearly found that the size distribution and nanostructure of the Ru/Ni/Ni(OH)$_2$/C catalyst were unchanged, suggesting that Ru/Ni/Ni(OH)$_2$/C was relatively stable during the reaction under mild conditions.

In addition, the HAADF-STEM images and elemental analysis results of Ru/Ni/Ni(OH)$_2$/C are present in Fig. S5 and S6.† As depicted, the Ru/Ni/Ni(OH)$_2$ NPs feature isolated Ru and Ni-containing NPs (Ru-on-Ni).

3.3 Synchrotron high energy X-ray diffraction (HE-XRD) data of the nanocatalysts

To gain further insights into the atomic structure of Ru/Ni/Ni(OH)$_2$/C, synchrotron high energy X-ray diffraction (HE-XRD) coupled with atomic pair distribution function (PDF) analysis was conducted. A representative set of experimental (PDF) data is shown in Fig. 2 and S7,† with PDF data of Ru/Ni/NiO/C also given for comparative purposes. Control samples such as Ru/C, Ni/NiO/C and Ni/Ni(OH)$_2$/C were also analyzed (see Fig. S8†). Analysis of the experimental PDFs revealed that Ru/Ni/Ni(OH)$_2$/C is a multi-phase mixture of metal oxides, metals and metal hydroxides including 25% NiO, 34% (Ni + Ru) metals, 18%

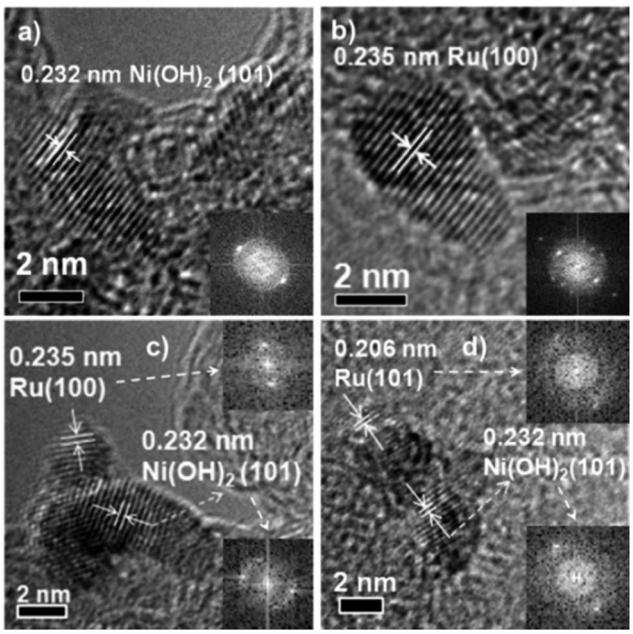

Fig. 1 HRTEM images of (a) Ni/Ni(OH)$_2$/C, (b) Ru/C, and (c and d) Ru/Ni/Ni(OH)$_2$/C. Scale bar: 2 nm. Insets: fast Fourier transform (FFT) patterns.

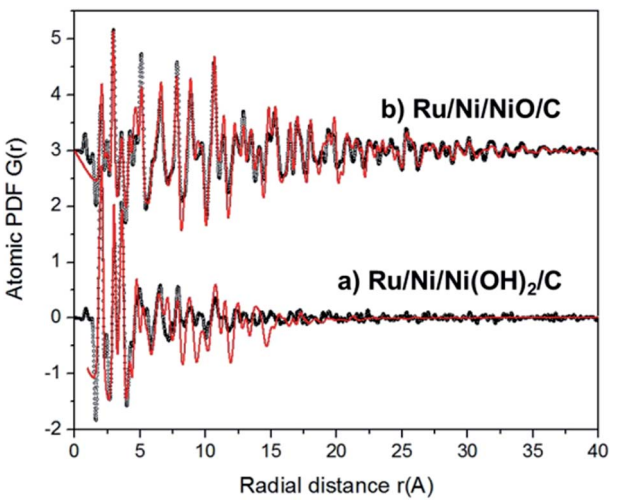

Fig. 2 (a) Atomic PDFs of (a) Ru/Ni/Ni(OH)$_2$/C and (b) Ru/Ni/NiO/C. Black curves: experimental PDFs; red curves: theoretical PDFs fitting the experimental PDFs.

$Ni(OH)_2$ and 23% RuO_2. Ru/Ni/NiO/C appeared as a mixture of 72% NiO, 6% $Ni(OH)_2$ and 20% (Ni + Ru) metals. Notably, the percentage of RuO_2 in the catalyst decreased dramatically to 2%, while the relative amount of NiO increased. The reason is possibly related to a much higher dispersion of Ru species on the surface of Ru/Ni/$Ni(OH)_2$/C as compared to that on the surface of Ru/Ni/NiO/C, resulting in Ru(0) being more easily oxidized in air. The surface RuO_2 with high dispersion could be however reduced to Ru(0) during the hydrogenation reaction at relatively low temperature in the Ru–Ni bimetallic catalyst. These results clearly confirmed the presence of nanostructured Ru nanoclusters supported on Ni/$Ni(OH)_2$ NPs in Ru/Ni/$Ni(OH)_2$/C.

3.4 HS-LEIS analysis of the nanocatalysts

To obtain the outermost surface atomic composition of the catalysts, HS-LEIS tests were performed with results displayed in Fig. 3. The signal of Ru atoms was detected on the outermost surface of Ru/C and Ni atoms in Ni/$Ni(OH)_2$/C in the 5 keV $^{20}Ne^+$ HS-LEIS spectra. For Ru/Ni/$Ni(OH)_2$/C, Ru and Ni atoms are present on the outermost surface. Obviously, the amount of Ni atoms on the outer surface of Ni/$Ni(OH)_2$/C is much larger with respect to that measured for Ru/Ni/$Ni(OH)_2$/C. We speculate that the main reason for this is that some Ni atoms have been fully covered by Ru nanoclusters in Ru/Ni/$Ni(OH)_2$/C.

3.5 X-ray absorption spectroscopic results of the nanocatalysts

With the purpose of investigating the relationship between the catalytic performance and the surface structure as well as the atomic-scale coordination structures of Ru and Ni-based catalysts, Ni K-edge XAS (X-ray Absorption Spectroscopy) tests were carried out for Ni/$Ni(OH)_2$/C and Ru/Ni/$Ni(OH)_2$/C, with XANES results shown in Fig. 4a. Combining with the reference compounds NiO and $Ni(OH)_2$, these spectra suggest that the average oxidation state of Ni atoms in Ni/$Ni(OH)_2$/C is close to +2. Based on preliminary visual analysis, the absorption edge of Ru/Ni/$Ni(OH)_2$/C is shifted towards higher energies, and there is an increased intensity in the white line (~8350 eV) in comparison with that of Ni/$Ni(OH)_2$/C. These features could indicate that Ni species in Ru/Ni/$Ni(OH)_2$/C are also present at a higher oxidation state when compared to non-Ru-based catalysts. This could be explained by the fact that a certain amount of Ni(0) atoms was replaced with Ru(0) atoms after Ru/Ni/$Ni(OH)_2$/C was obtained *via* galvanic replacement. Fig. 4b displays the Ru K-edge XANES spectra of Ru/C and Ru/Ni/$Ni(OH)_2$/C. The results suggested that the Ru oxidation state, RuO_2, and Ru reduced state, Ru(0), co-exist in these two samples after comparison with the Ru K-edge XANES spectra of the reference compounds (RuO_2 and Ru foil). However, the average oxidation number of Ru atoms in Ru/Ni/$Ni(OH)_2$/C is clearly much larger than that of Ru/C. This can further indicate that Ru atoms in Ru/Ni/$Ni(OH)_2$/C are mainly supported on the surface and easily oxidized in air due to higher dispersion with respect to those in Ru/C.

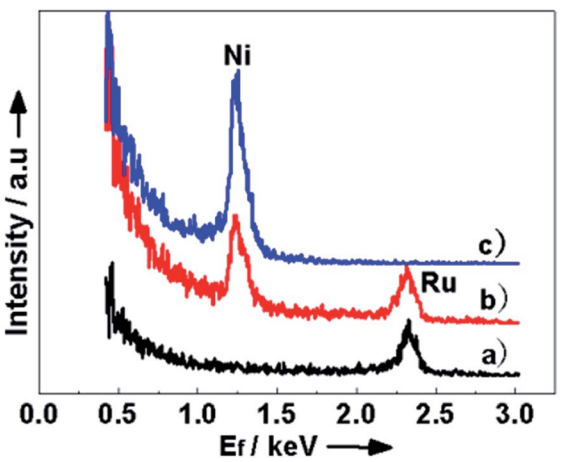

Fig. 3 5 keV $^{20}Ne^+$ HS-LEIS spectra of (a) Ru/C, (b) Ru/Ni/$Ni(OH)_2$/C and (c) Ni/$Ni(OH)_2$/C.

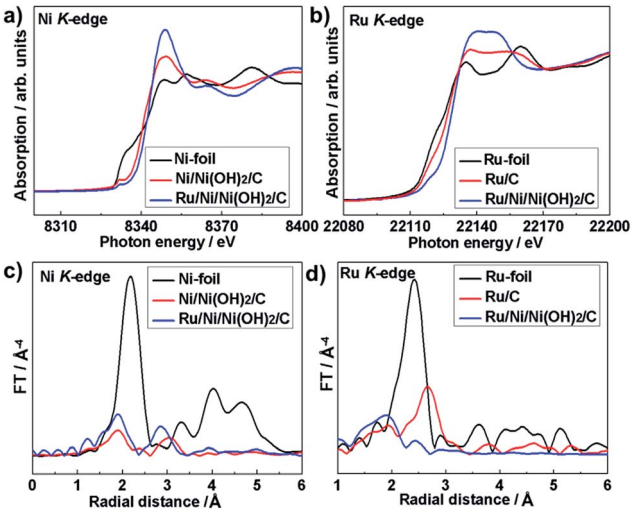

Fig. 4 X-ray absorption studies of the catalysts under ambient conditions. (a) XANES and (c) Fourier-transformed EXAFS spectra of Ni foil, Ni/$Ni(OH)_2$/C and Ru/Ni/$Ni(OH)_2$/C catalysts recorded at the Ni K-edge; (b) XANES and (d) Fourier-transformed EXAFS spectra of Ru foil, Ru/C and Ru/Ni/$Ni(OH)_2$/C catalysts recorded at the Ru K-edge.

Fig. 4c shows the Fourier transform of the EXAFS (Extended X-ray Absorption Fine Structure) spectra at the Ni K-edge of Ni/$Ni(OH)_2$/C and Ru/Ni/$Ni(OH)_2$/C along with Ru foil. Due to a relatively large portion of surface atoms with unsaturated coordination, nano-scaled particles always possess a smaller number of neighboring atoms on average so that Ni/$Ni(OH)_2$/C and Ru/Ni/$Ni(OH)_2$/C exhibited much weaker EXAFS oscillations (and hence weaker FT peaks) with respect to the bulk structure of reference compounds. For Ni/$Ni(OH)_2$/C and Ru/Ni/$Ni(OH)_2$/C, except for the first and second coordination shell, the EXAFS contributions from higher shells are almost absent, indicating a very high dispersion of Ni atoms. Most Ni atoms in these two samples remained in the oxidized state. The Ni^{2+}/Ni(0) atomic ratio in Ru/Ni/$Ni(OH)_2$/C was found to be obviously larger than that in Ni/$Ni(OH)_2$/C, which is consistent with the normalized XANES spectra at the Ni K-edge obtained for these two samples.

Table 2 Best-fit EXAFS parameters of the Ru/Ni/Ni(OH)$_2$/C, Ni/Ni(OH)$_2$/C and Ru/C samples

Catalyst	Scattering path	r (Å)	CN	$2\sigma^2$/Å^2	E_F (eV)	R_f (Å)	k range (Å^{-1}) R range (Å)
Ru/Ni/Ni(OH)$_2$/C Ru K-edge	Ru–O	2.00 (2)	4.8 (5)	0.0075 (1)	−3.7	0.0057	k: 3–11, R: 1.2–3.4
	Ru–Ni	2.54 (5)	0.8 (4)	0.0030 (2)			
	Ru–Ru	2.56 (4)	1.5 (4)	0.0046 (1)			
	Ru–Ru	3.10 (4)	0.8 (2)	0.0050			
Ru/Ni/Ni(OH)$_2$/C Ni K-edge	Ni–O	2.04 (1)	3.9 (5)	0.0060 (1)	−5.6	0.0045	k: 3–11, R: 1–3.6
	Ni–Ni	2.99 (1)	4.8 (7)	0.0120 (3)			
Ni/Ni(OH)$_2$/C Ni K-edge	Ni–O	2.04 (1)	2.1 (2)	0.0048 (1)	−1.4	0.0046	k: 3–12, R: 1–3.0
	Ni–Ni	2.34 (3)	0.5 (1)	0.010 (2)			
	Ni–Ni	3.08 (1)	2.9 (5)	0.011 (1)			
Ru/C Ru K-edge	Ru–O	1.98 (1)	2.8 (3)	0.0069 (1)	−4.2	0.010	k: 3–14, R: 1–4
	Ru–Ru	2.68 (2)	5.3 (5)	0.0046 (2)			
	Ru–Ru	3.78 (2)	2.4 (6)	0.0050 (1)			

Fourier transformation of k^3-weighted EXAFS oscillations at the Ru K-edge of Ni/Ni(OH)$_2$/C, Ru/Ni/Ni(OH)$_2$/C and Ru foil is also shown in Fig. 4d. According to the strength of EXAFS oscillations, it can be found that the size of Ru particles in Ru/Ni/Ni(OH)$_2$/C is much smaller than that in Ru/C, and the Ru dispersion in Ru/Ni/Ni(OH)$_2$/C is much better than that in Ru/C.

The structural and statistical information derived from each sample is listed in Table 2 (see detailed analysis in the ESI†). For Ni/Ni(OH)$_2$/C, a distance of 2.34 Å and 3.08 Å (shorter than the Ni–Ni bonding distance in Ni foil) represented Ni–Ni contributions with an average coordination number (CN) of 0.5 and 2.9, respectively. The presence of Ni–O contributions was detected with an average coordination number of 2.1. The average CN of the Ni–Ni/Ni–O ratio in Ni/Ni(OH)$_2$/C was larger than that in Ru/Ni/Ni(OH)$_2$/C, implying that Ni(0) nanoclusters were probably loaded on Ni(OH)$_2$ NPs in these two samples. For the Ru/C catalyst, the average CN of Ru–Ru bonds with a distance of 2.68 Å and 3.78 Å was 5.3 and 2.4, respectively. A distance of 1.98 Å was attributed to Ru–O bonding with a CN of 2.8. However, a much larger Ru–O coordination number (4.8) was observed for Ru/Ni/Ni(OH)$_2$/C as compared to Ru/C, suggesting that the major Ru species are present in the oxidized form under ambient conditions. Most importantly, the observed distance of 2.54 Å could be assigned to Ru–Ni bonds with a CN of 0.8. These findings support the deposition of Ru nanoclusters on the surface of Ni/Ni(OH)$_2$ NPs (Ru nanoclusters-on-Ni/Ni(OH)$_2$ NPs) in Ru/Ni/Ni(OH)$_2$/C, which is in good agreement with other characterization results described in this work.

CN, coordination number; r, distance between absorber and backscatter atoms; σ^2, Debye–Waller factor value; k and R, data range for fitting in k-space and R-space, respectively; R_f, R-factor characterizing the goodness of fit; E_F, inner potential correction accounting for the difference in the inner potential between the sample and the reference compound.

The comprehensive structural investigations using a variety of characterization techniques proved that Ru/Ni/Ni(OH)$_2$/C is composed of Ru nanostructures (isolated nanoclusters) loaded on Ni/Ni(OH)$_2$ NPs. The Ru nanoclusters were stabilized by the strong interface synergetic interactions among Ru, Ni and Ni(OH)$_2$. These features rendered Ru/Ni/Ni(OH)$_2$/C as a remarkable catalytic system for room temperature naphthalene hydrogenation in comparison to Ru/C, Ni/Ni(OH)$_2$/C, and Ru–Ni alloy/C, which exhibited negligible activity. The proposed mechanism of this synergy can be described as follows: (1) naphthalene is preferentially adsorbed and activated on accessible Ni(OH)$_2$ sites. (2) Hydrogen is easily adsorbed and dissociates at Ru sites, forming activated H* species due to the effectiveness of noble metals in hydrogen activation. (3) Ni sites located between Ru and Ni(OH)$_2$ play a vital role in transferring H* to Ni(OH)$_2$ sites (as a "bridge") by hydrogen spillover.[41–43] (4) The activated naphthalene is hydrogenated by the activated H* species on Ru sites, forming decalin.

4 Conclusions

In conclusion, nanostructured Ru nanoclusters supported on the surface of Ni/Ni(OH)$_2$ NPs and loaded on carbon were designed and prepared *via* hydrazine hydrate reduction and galvanic replacement. An interface synergetic effect of Ru, Ni and Ni(OH)$_2$ sites largely improved the catalytic activity of Ru/Ni/Ni(OH)$_2$/C for naphthalene hydrogenation, which was comparably higher to that of Ru/C, Ni/Ni(OH)$_2$/C and Ru–Ni alloy/C. This study is a classic example to illustrate the concept of designing a highly efficient nanocatalyst – a noble metal (NM) nanoclusters-on-transition metal (TM)-on-transition metal oxide (TMO) or transition metal hydroxide (TMOH) NP hybrid for hydrogenation reactions. The proposed approach to design multi-metallic nanocatalysts can take full advantage of metal atoms (especially precious metal atoms) towards advancing the development of multifunctional materials for catalytic applications.

Acknowledgements

The authors would like to thank the Natural Science Foundation of Jiangxi Province of China (Grant No. 20161BAB213083), Research Foundation of the Education Bureau of Jiangxi Province of China (GJJ160666), and National Natural Science Foundation of China (Grant No. 21303140, 21466013, 51371178 and 51390473). Diamond Light Source is gratefully acknowledged for rapid access to the facility for EXAFS measurement on B18. The HE-XRD work was supported by DOE-BES Grant DE-SC0006877.

Work at the Advanced Photon Source was supported by DOE under Contract DEAC02-06CH11357.

Notes and references

1 P. A. Rautanen, M. S. Lylykangas, J. R. Aittamaa and A. O. I. Krause, *Ind. Eng. Chem. Res.*, 2002, **41**, 5966–5975.
2 M. Zahmakıran, Y. Tonbul and S. Özkar, *J. Am. Chem. Soc.*, 2010, **132**, 6541–6549.
3 Y. Tonbul, M. Zahmakiran and S. Özkar, *Appl. Catal., B*, 2014, **148–149**, 466–472.
4 S. Miao, Z. Liu, B. Han, J. Huang, Z. Sun, J. Zhang and T. Jiang, *Angew. Chem., Int. Ed.*, 2006, **45**, 266–269.
5 A. Nowicki, Y. Zhang, B. Léger, J. P. Rolland, H. Bricout, E. Monflier and A. Roucoux, *Chem. Commun.*, 2006, 296–298.
6 A. Roucoux, J. Schulz and H. Patin, *Adv. Synth. Catal.*, 2003, **345**, 222–229.
7 L. Zhu, H. Sun, J. Zheng, C. Yu, N. Zhang, Q. Shu and B. H. Chen, *Mater. Chem. Phys.*, 2017, **192**, 8–16.
8 M. Pang, C. Liu, W. Xia, M. Muhler and C. Liang, *Green Chem.*, 2012, **14**, 1272–1276.
9 M. Shirai, C. V. Rode, E. Mine, A. Sasaki, O. Sato and N. Hiyoshi, *Catal. Today*, 2006, **115**, 248–253.
10 X. Ma, K. Sakanishi, T. Isoda and I. Mochida, *Energy Fuels*, 1995, **9**, 33–37.
11 C. Song, *Catal. Today*, 2003, **86**, 211–263.
12 A. Stanislaus and B. H. Cooper, *Catal. Rev.*, 1994, **36**, 75–123.
13 B. H. Cooper and B. B. L. Donnis, *Appl. Catal., A*, 1996, **137**, 203–223.
14 A. J. Suchanek, *Oil Gas J.*, 1990, **88**, 109–119.
15 S. R. Kirumakki, B. G. Shpeizer, G. V. Sagar, K. V. Chary and A. Clearfield, *J. Catal.*, 2006, **242**, 319–331.
16 H. Chen, H. Yang, O. Omotoso, L. Ding, Y. Briker, Y. Zheng and Z. Ring, *Appl. Catal., A*, 2009, **358**, 103–109.
17 P. Zhang, T. Wu, M. Hou, J. Ma, H. Liu, T. Jiang, W. Wang, C. Wu and B. Han, *ChemCatChem*, 2014, **6**, 3323–3327.
18 I. S. Park, M. S. Kwon, N. Kim, J. S. Lee, K. Y. Kang and J. Park, *Chem. Commun.*, 2005, 5667–5669.
19 M. Jacquin, D. J. Jones, J. Rozière, S. Albertazzi, A. Vaccari, M. Lenarda, L. Storaro and R. Ganzerla, *Appl. Catal., A*, 2003, **251**, 131–141.
20 S. Albertazzi, G. Busca, E. Finocchio, R. Glöckler and A. Vaccari, *J. Catal.*, 2004, **223**, 372–381.
21 G. Chen, Y. Zhao, G. Fu, P. N. Duchesne, L. Gu, Y. Zheng, X. Weng, M. Chen, P. Zhang, C.-W. Pao, J.-F. Lee and N. Zheng, *Science*, 2014, **344**, 495–499.
22 L. Zhu, Y. Jiang, J. Zheng, N. Zhang, C. Yu, Y. Li, C.-W. Pao, J.-L. Chen, C. Jin, J.-F. Lee, C.-J. Zhong and B. H. Chen, *Small*, 2015, **11**, 4385–4393.
23 G. Kyriakou, M. B. Boucher, A. D. Jewell, E. A. Lewis, T. J. Lawton, A. E. Baber, H. L. Tierney, M. Flytzani-Stephanopoulos and E. C. H. Sykes, *Science*, 2012, **335**, 1209–1212.
24 C. Li, J. Zhou, W. Gao, J. Zhao, J. Liu, Y. Zhao, M. Wei, D. G. Evans and X. Duan, *J. Mater. Chem. A*, 2013, **1**, 5370–5376.
25 I. X. Green, W. Tang, M. Neurock and J. T. Yates, *Science*, 2011, **333**, 736–739.
26 Y. Huang, Y. Ma, Y. Cheng, L. Wang and X. Li, *Catal. Commun.*, 2015, **69**, 55–58.
27 R. R. Deshmukh, J. W. Lee, U. S. Shin, J. Y. Lee and C. E. Song, *Angew. Chem., Int. Ed.*, 2008, **47**, 8615–8617.
28 J. M. Hodges, J. R. Morse, M. E. Williams and R. E. Schaak, *J. Am. Chem. Soc.*, 2015, **137**, 15493–15500.
29 J. M. Hodges, A. J. Biacchi and R. E. Schaak, *ACS Nano*, 2014, **8**, 1047–1055.
30 Y. Huang, Y. Ma, Y. Cheng, L. Wang and X. Li, *Ind. Eng. Chem. Res.*, 2014, **53**, 4604–4613.
31 D. Chen, P. Sun, H. Liu and J. Yang, *J. Mater. Chem. A*, 2017, **5**, 4421–4429.
32 J. Zhang, K. Sasaki, E. Sutter and R. R. Adzic, *Science*, 2007, **315**, 220–222.
33 J. Liu, B. Chen, Y. Kou, Z. Liu, X. Chen, Y. Li, Y. Deng, X. Han, W. Hu and C. Zhong, *J. Mater. Chem. A*, 2016, **4**, 11060–11068.
34 N. Jung, Y. Sohn, J. H. Park, K. S. Nahm, P. Kim and S. J. Yoo, *Appl. Catal., B*, 2016, **196**, 199–206.
35 T. Fu, J. Fang, C. Wang and J. Zhao, *J. Mater. Chem. A*, 2016, **4**, 8803–8811.
36 M. Kim, S. M. Ko and J. M. Nam, *Nanoscale*, 2016, **8**, 11707–11717.
37 L. Zhu, Z. Yang, J. Zheng, W. Hu, N. Zhang, Y. Li, C.-J. Zhong, H. Ye and B. H. Chen, *J. Mater. Chem. A*, 2015, **3**, 124–132.
38 V. Petkov, *Mater. Today*, 2008, **11**, 28–38.
39 http://cars9.uchicago.edu/~ravel/software/aboutathena.html.
40 http://bruceravel.github.io/demeter/.
41 W. C. Conner Jr and J. L. Falconer, *Chem. Rev.*, 1995, **95**, 759–788.
42 R. Prins, *Chem. Rev.*, 2012, **112**, 2714–2738.
43 W. Karim, C. Spreafico, A. Kleibert, J. Gobrecht, J. VandeVondele, Y. Ekinci and J. A. van Bokhoven, *Nature*, 2017, **541**, 68–71.